Nanoscale

PAPER

View Article Online
View Journal | View Issue

Cite this: *Nanoscale*, 2016, **8**, 9805

Probing the structures of gold–aluminum alloy clusters $Au_xAl_y^-$: a joint experimental and theoretical study†

Navneet Singh Khetrapal,‡[a] Tian Jian,‡[b] Rhitankar Pal,[a] Gary V. Lopez,[b] Seema Pande,[a] Lai-Sheng Wang*[b] and Xiao Cheng Zeng*[a]

Received 23rd February 2016,
Accepted 1st April 2016

DOI: 10.1039/c6nr01506a

www.rsc.org/nanoscale

Besides the size and structure, compositions can also dramatically affect the properties of alloy nanoclusters. Due to the added degrees of freedom, determination of the global minimum structures for multi-component nanoclusters poses even greater challenges, both experimentally and theoretically. Here we report a systematic and joint experimental/theoretical study of a series of gold–aluminum alloy clusters, $Au_xAl_y^-$ ($x + y = 7,8$), with various compositions ($x = 1–3$; $y = 4–7$). Well-resolved photoelectron spectra have been obtained for these clusters at different photon energies. Basin-hopping global searches, coupled with density functional theory calculations, are used to identify low-lying structures of the bimetallic clusters. By comparing computed electronic densities of states of the low-lying isomers with the experimental photoelectron spectra, the global minima are determined. It is found that for $y \geq 6$ there is a strong tendency to form the magic-number square bi-pyramid motif of Al_6^- in the $Au_xAl_y^-$ clusters, suggesting that the Al–Al interaction dominates the Au–Au interaction in the mixed clusters. A closely related trend is that for $x > 1$, the gold atoms tend to be separated by Al atoms unless only the magic-number Al_6^- square bi-pyramid motif is present, suggesting that in the small-sized mixed clusters, Al and Au components do not completely mix with one another. Overall, the Al component appears to play a more dominant role due to the high robustness of the magic-number Al_6^- square bi-pyramid motif, whereas the Au component tends to be either "adsorbed" onto the Al_6^- square bi-pyramid motif if $y \geq 6$, or stays away from one another if $x < y < 6$.

1 Introduction

The study of metal clusters has been an active area of research as metal clusters can possess properties dramatically different from the bulk counterpart on the one hand and the atomic states on the other. The size- and structure-dependent properties of the pure metal clusters render them attractive models for catalysis, sensors, as well as a fertile ground for developing new nanomaterials. Furthermore, the properties of metal clusters can be extended by adding more components of metal elements. The additional degrees of freedom in stoichiometry can offer increased versatility in tuning the properties of alloy clusters. However, the added degrees of freedom also pose greater challenges in determining the composition-dependent global minima, both experimentally and theoretically. Importantly, alloy clusters are expected to have structures and properties different from those of the constituent elemental clusters, as well as those of the bulk alloys. Among the metal clusters reported in the literature, both gold and aluminum clusters have received considerable attention. Previous studies have established that small-sized gold cluster anions exhibit two-dimensional (2D) structures until Au_{11}^-, and that there exists the 2D–3D structural transition at Au_{12}^-.[1] On the other hand, for pure aluminum cluster anions, 2D structures are favored until Al_5^-, beyond which 3D structures arise.[2] Several bare gold or bare aluminum cluster anions are shown to exhibit highly symmetric structures, such as the Au_{16}^- golden cage and the tetrahedral Au_{20}^- pyramid, as well as the icosahedral Al_{13}^-.[2–6] The structures and properties of the small-sized clusters can vary drastically even if only a single atom is replaced by a different metal atom.

Here, our joint experimental/theoretical study is focused on the bimetallic clusters consisting of Au and Al. The low cost

[a]*Department of Chemistry and Nebraska Center for Materials and Nanoscience, University of Nebraska-Lincoln, Lincoln, Nebraska 68588, USA.*
E-mail: xzeng1@unl.edu
[b]*Department of Chemistry, Brown University, Providence, RI 02912, USA.*
E-mail: lai-sheng_wang@brown.edu
†Electronic supplementary information (ESI) available. See DOI: 10.1039/c6nr01506a
‡These authors contributed equally to this work.

and high abundance of aluminum render it a viable dopant in making novel Au–Al alloy nanoclusters. Several experimental studies have been previously reported on the Au–Al alloy clusters. Two mass-spectrometry studies demonstrated the electronic shell effects on Au–Al cation clusters.[7,8] The first photoelectron spectroscopy (PES) study of Au–Al alloy clusters indicates that $AuAl_6^-$ can be viewed as building upon the O_h-Al_6^{2-} structure with the Au^+ coordinated to one face of Al_6^{2-}.[9] Another theoretical study suggests that Au_5Al prefers a 3D structure.[10] Later, a joint experimental/theoretical work shows that $AuAl_6^-$ is exceptionally stable with a 20-electron closed shell and thus can resist the etching of oxygen.[11] A combined PES and density functional theory (DFT) study of $AuAl_{12}^-$ shows that the Au atom tends to stay in the center of a distorted Al_{12}^- cage.[12] A theoretical study of the $AuAl_7$ cluster suggests that it possesses a large gap between the highest occupied molecular orbital (HOMO) and the lowest unoccupied molecular orbital (LUMO).[13] Several DFT studies explored the structural and electronic properties of gold clusters doped with one and two aluminum atoms, suggesting that the Al dopants can dramatically change the structures of the host gold clusters.[14–16] Recently, a DFT study of $AuAl_n$ (n = 1–15) clusters indicated that the Au atom tends to occupy a peripheral position in these clusters.[17] Very recently, a combined high-resolution PES and DFT study demonstrated that both $Au_2Al_2^-$ and Au_2Al_2 possess C_{2v} tetrahedral structures.[18]

In this article, we report a joint PES and theoretical investigation of the structures of a series of gold–aluminum alloy cluster anions, namely, $Au_xAl_y^-$ ($x + y$ = 7,8; x = 1–3; y = 4–7), over a range of compositions. Note that several aluminum-doped or mixed gold clusters have been studied previously.[19–29] To our knowledge, however, this is the first systematic experimental/theoretical investigation of the global minimum structures of Au–Al alloy clusters with changing size and composition.

2 Experimental and theoretical methods

2.1 Photoelectron spectroscopy

The experiment was carried out using a magnetic-bottle PES apparatus equipped with a laser vaporization cluster source, details of which have been published elsewhere.[30] Briefly, the gold–aluminum anions were produced by laser vaporization of an Al/Au mixed target with helium carrier gas seeded with 5% argon. The anions of interest were each mass-selected and decelerated before being photodetached by a pulsed laser beam. Photoelectrons were collected at nearly 100% efficiency by using a magnetic bottle and analyzed in a 3.5 m long electron flight tube. The photodetachment experiment was conducted at three detachment photon energies: 355 nm (3.496 eV) and 266 nm (4.661 eV) from a Nd:YAG laser, and 193 nm (6.424 eV) from an ArF excimer laser. Photoelectron spectra were calibrated by using the known spectra of Au^- and Bi^-, and the energy resolution of the apparatus was $\Delta E_k/E_k \approx 2.5\%$, that is, approximately 25 meV for 1 eV electrons.

2.2 Theoretical methods

The basin-hopping (BH) global optimization method in conjunction with DFT calculations was used for the search of global minimum structures of the gold–aluminum alloy clusters. During the BH search, after each accepted move the resulting local minimum geometry was further optimized using generalized gradient approximation (GGA) with the Perdew–Burke–Ernzerhof (PBE) exchange correlation functional[31] and the double-numerical polarized (DNP) basis set with effective core potential (ECP), implemented in a Dmol^3 4.0 program.[32,33] The top 20 low-lying isomers thus obtained from the BH global optimization were considered as candidates for the lowest-energy structure. These candidates were further re-optimized using meta-GGA M06 functional[34] with the aug-cc-pVDZ basis set,[35] implemented in the G09 package.[36] During the re-optimization, some of the structures converged to the same geometry. This reduced the number of isomers to 6–15 for each cluster. Next, single-point energy calculations of the optimized geometries were performed using PBE0 functional[37] (with aug-cc-pVTZ basis for aluminum and CRENBL-ECP for gold) implemented in NWCHEM 6.3 package,[38] with the inclusion of the spin–orbit (SO) effects for the gold. The theoretical adiabatic detachment energy (ADE) for each isomer was calculated as the energy difference between the ground state of the anion and that of the neutral. Theoretical vertical detachment energies (VDEs) were calculated using the time-independent DFT method. The first VDE was calculated as the energy difference between the neutral and the anion at the optimized anion geometry. The higher VDEs were approximated by adding vertical excitation energies to the first VDE. The ADE and VDE calculations were done at the PBE0/(Al/aug-cc-pVTZ, Au/CRENBL-ECP) level. Each VDE was fitted with a 0.035 eV Gaussian width to yield the simulated PES spectrum. The simulated spectra were then compared with the experimental spectra to identify the lowest-energy structures. In addition, the CCSD(T)[39] (coupled-cluster method including singles, doubles and noniterative perturbative triple) calculations with the cc-pVTZ basis set,[40] implemented in the G09 package, were also performed to ascertain the best isomer in cases where more than one candidate closely matched the experimental spectrum.

3 Results

3.1 Experimental results

The photoelectron spectra of $Au_xAl_y^-$ ($x + y$ = 7,8; x = 1–3; y = 4–7) are shown in Fig. 1 at three detachment photon energies: 355 nm (3.496 eV), 266 nm (4.661 eV), and 193 nm (6.424 eV). The observed detachment transitions are labeled by letters: X, A, B, C, *etc*. Weak features labeled as X′ and A′ in some spectra indicate contributions from minor isomers. The vertical detachment energies (VDEs) for the observed features are listed in ESI Tables S1–S6.† In each spectrum, the X band stands for the transition from the ground state of the anion to that of the neutral. The A, B, *etc.* bands denote the transitions to the excited states of the neutral species.

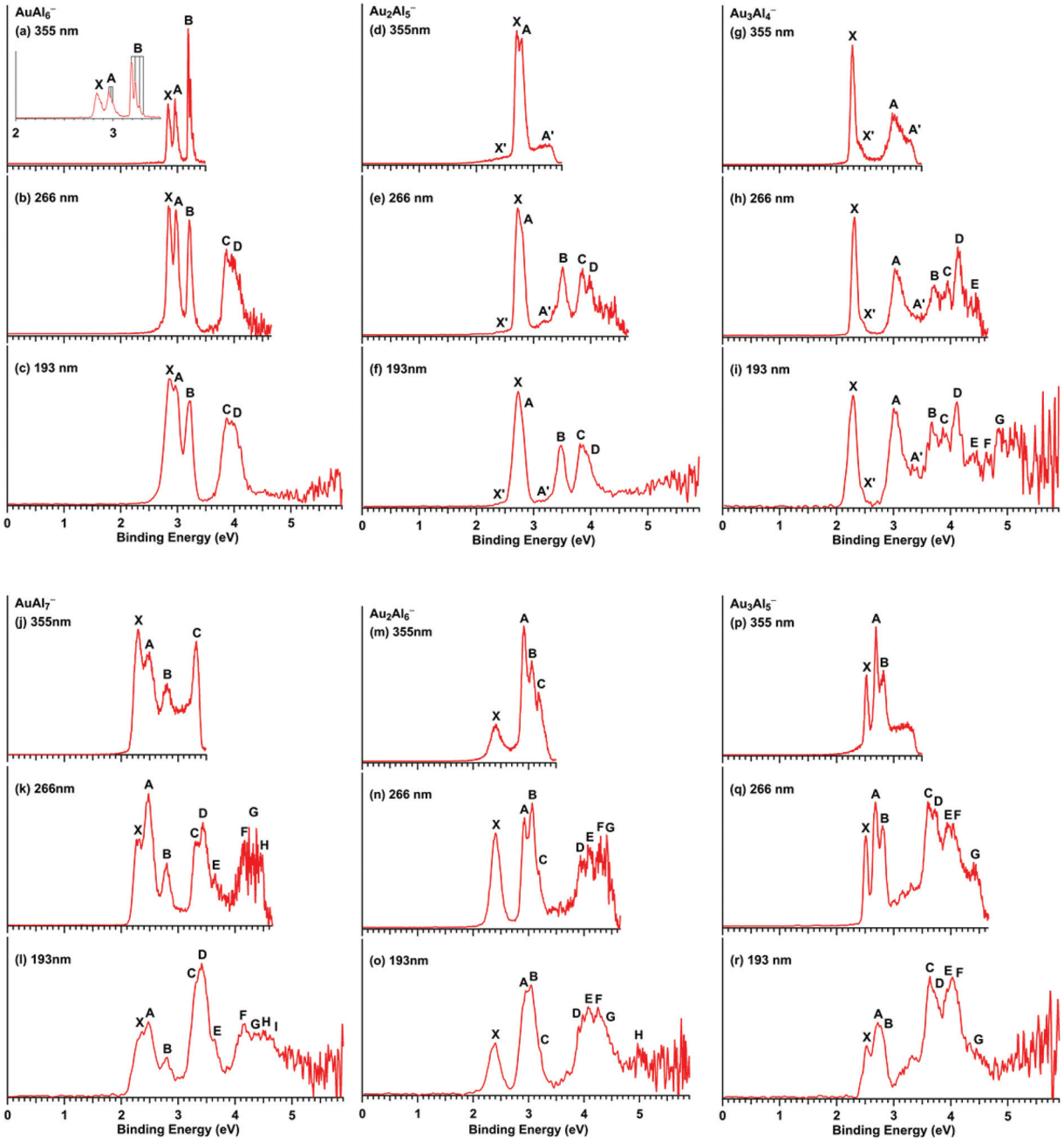

Fig. 1 Experimental photoelectron spectra of $Au_xAl_y^-$ ($x + y = 7,8$; $x = 1–3$; $y = 4–7$) at three photon energies. The vertical lines in the inset in (a) represent resolved vibrational structures.

$AuAl_6^-$. The spectra of $AuAl_6^-$ have been reported before[9] and they are included here for completeness and comparison. The data presented in Fig. 1 were retaken for this study along with the other $Au_xAl_y^-$ species. The new data are similar to those published previously. The $AuAl_6^-$ cluster was the only cluster for which we were able to resolve vibrational structures (Fig. 1a). All the VDEs given in ESI Table S1† are also similar to those reported previously. It should be noted that band D, which overlaps with band C, was labeled as C′ in the earlier report.[9]

$Au_2Al_5^-$. The 355 nm spectrum of $Au_2Al_5^-$ (Fig. 1d) reveals two prominent and closely-spaced bands (X, A) and two weak bands (X′, A′). The VDEs of band X and band A are observed at 2.71 eV and 2.80 eV, respectively. A broad tail (X′) is shown on the lower binding energy side of the ground-state detachment band X, and it likely stems from a low-lying isomer or vibrational hot bands. A weak, broad feature A′ is observed on the higher binding energy side. As shown in the spectra of $AuAl_6^-$, the clusters under our experimental conditions are quite cold so that hot bands can be excluded. The weak X′ and A′ features are most likely due to a low-lying isomer. At 266 nm (Fig. 1e), three more bands, B, C and D, are resolved. At 193 nm (Fig. 1f), no more resolved features are observed,

except for weak continuous signals on the high binding energy side. The spectra of $Au_2Al_5^-$ suggest that they are from a major isomer with minor contributions from a low-lying isomer. All the observed VDEs for $Au_2Al_5^-$ are given in ESI Table S2.†

$Au_3Al_4^-$. The 355 nm spectrum (Fig. 1g) of $Au_3Al_4^-$ reveals a very sharp and intense ground state peak X, well separated from a broader band A. In addition, two weak shoulders appear on the higher binding energy side of the major X and A bands (X′, A′). The 266 nm spectrum (Fig. 1h) of $Au_3Al_4^-$ reveals numerous closely-spaced PES bands (B–E) in the higher binding energy region. The 193 nm spectrum (Fig. 1i) displays even more complicated spectral features at higher binding energies. Peaks E, F, and G can be tentatively identified. Beyond band G, the 193 nm spectrum exhibits almost continuous signals with poor signal-to-noise ratios. The four weak bands (X′, A′, E, and F) may come from a low-lying isomer or two-electron processes.[30] Since the relative intensities of bands X′ and A′ show no photon energy dependence, they are likely from a low-lying isomer. The spectra of $Au_3Al_4^-$ suggest that they consist of a major isomer and a weakly populated isomer, similar to the case of $Au_2Al_5^-$. All the measured VDEs of $Au_3Al_4^-$ are given in ESI Table S3.†

$AuAl_7^-$. The 355 nm spectrum (Fig. 1j) of $AuAl_7^-$ displays four intense and not well-separated PES bands (X, A–C), where band C seems to be cut due to the low photon energy. In the 266 nm spectrum (Fig. 1k), a more intense band D is observed, which overlaps with band C with a weak shoulder E on the higher binding energy side of band D. Highly congested spectral features are observed on the high binding energy side in Fig. 1k and continue in the 193 nm spectrum (Fig. 1l), with tentatively labeled bands, F to I. It should be noted that the relative intensities of a number of PES bands for $AuAl_7^-$ show strong photon energy dependence. The complex spectral features may also suggest the possible presence of a minor low-lying isomer. All the obtained VDEs for $AuAl_7^-$ are given in ESI Table S4.†

$Au_2Al_6^-$. The 355 nm spectrum (Fig. 1m) of $Au_2Al_6^-$ shows a relatively broad and weak ground-state band (X), followed by three very sharp and overlapping bands (A–C). The separation between the X and A bands indicates a HOMO–LUMO gap of 0.51 eV for neutral Au_2Al_6. The 266 nm spectrum (Fig. 1n) of $Au_2Al_6^-$ reveals four more congested bands (D–G) with relatively poor signal-to-noise ratios. In the 193 nm spectrum (Fig. 1o), no more major PES bands are observed beyond band G, while a weak band H can be identified tentatively. The relative intensity of band X of $Au_2Al_6^-$ also displays interesting photon-energy dependence. All the experimental VDEs of $Au_2Al_6^-$ are given in ESI Table S5.†

$Au_3Al_5^-$. The 355 nm spectrum (Fig. 1p) of $Au_3Al_5^-$ shows three sharp bands (X, A and B), followed by weak continuous signals in the high binding energy region. These weak signals seem to consist of three resolved peaks in the 266 nm spectrum (Fig. 1q, not labeled). Apart from these weak peaks, the 266 nm spectrum reveals highly congested PES bands (C to G) on the higher binding energy side, following a large energy gap of ~0.8 eV from band B. The 193 nm spectrum (Fig. 1r) shows no more well-resolved bands, except for nearly continuous signals with poor signal-to-noise ratios. The weak features in the gap of bands B and C are likely due to either minor isomer contributions or two-electron processes.[30] All the measured VDEs for the main PES bands of $Au_3Al_5^-$ are given in ESI Table S6.†

Table 1 Experimental VDEs, ADEs, number of valence electrons (*N*), the gap between peaks X and A (H1–H2 gap) for $Au_xAl_y^-$ ($x + y = 7,8$; $x = 1–3$; $y = 4–7$). All energies are in eV

	VDE[a]	ADE[a]	*N*	H1–H2 gap
$AuAl_6^-$	2.83(3)	2.83(3)	20	0.13
$Au_2Al_5^-$	2.71(3)	2.65(3)	18	0.09
$Au_3Al_4^-$	2.28(4)	2.24(4)	16	0.71
$AuAl_7^-$	2.30(4)	2.19(4)	23	0.18
$Au_2Al_6^-$	2.41(4)	2.25(4)	21	0.51
$Au_3Al_5^-$	2.53(3)	2.51(3)	19	0.16

[a] Numbers in the parentheses represent uncertainties in the last digit.

3.1.1 Comparison of the electronic properties of $Au_xAl_y^-$. Table 1 lists the measured first VDEs, ADEs, number of valence electrons (1 for Au and 3 for Al) in the $Au_xAl_y^-$ anions, and the gap between bands X and A, which represents the energy difference between the top two highest occupied molecular orbitals (H1–H2 gap) for each cluster. $AuAl_6^-$ and $Au_2Al_5^-$ exhibit higher ADEs, probably because both clusters have closed-shell electron configurations (magic numbers) according to the jellium model. We see that in the case of the seven-atom clusters, the VDEs decrease from $AuAl_6^-$ to $Au_3Al_4^-$. In the case of the eight-atom clusters, the VDEs increase from $AuAl_7^-$ to $Au_3Al_5^-$.

3.2 Theoretical results and comparison with the experiment

The global minima of all the binary clusters were thoroughly searched (see the Experimental and theoretical methods section). The simulated PES spectra of the two or three lowest-lying isomers (based on the relative energies at M06/aug-ccpVDZ level of theory) are compared with the experimental spectra for each cluster shown in Fig. 2. The simulated spectra were obtained by fitting the computed VDEs with a unit area Gaussian function of 0.035 eV width. Other low-lying isomers and their simulated spectra can be found in Fig. SI–SVI.† The relative energies of all the low-lying isomers and their computed first VDEs are shown in Tables 2–7, for the six $Au_xAl_y^-$ clusters, respectively.

$AuAl_6^-$. The simulated spectra of the top-two lowest-lying isomers (I and II) of $AuAl_6^-$ are compared with the experimental spectrum shown in Fig. 2 (the top left panel). While isomers I and II are close in energy, the other isomers are too high in relative energy (Table 2) and they all can be excluded. It should be mentioned that the global minimum structure (isomer I) is in agreement with the previous studies.[9,11,17] Even though the computed first VDE and ADE of isomers I and II compare well with experimental data, the overall simulated spectrum of the global minimum isomer I is clearly in best agreement with the experimental spectrum. Isomer II can also be ruled out on the basis of its relatively high energy (0.154 eV

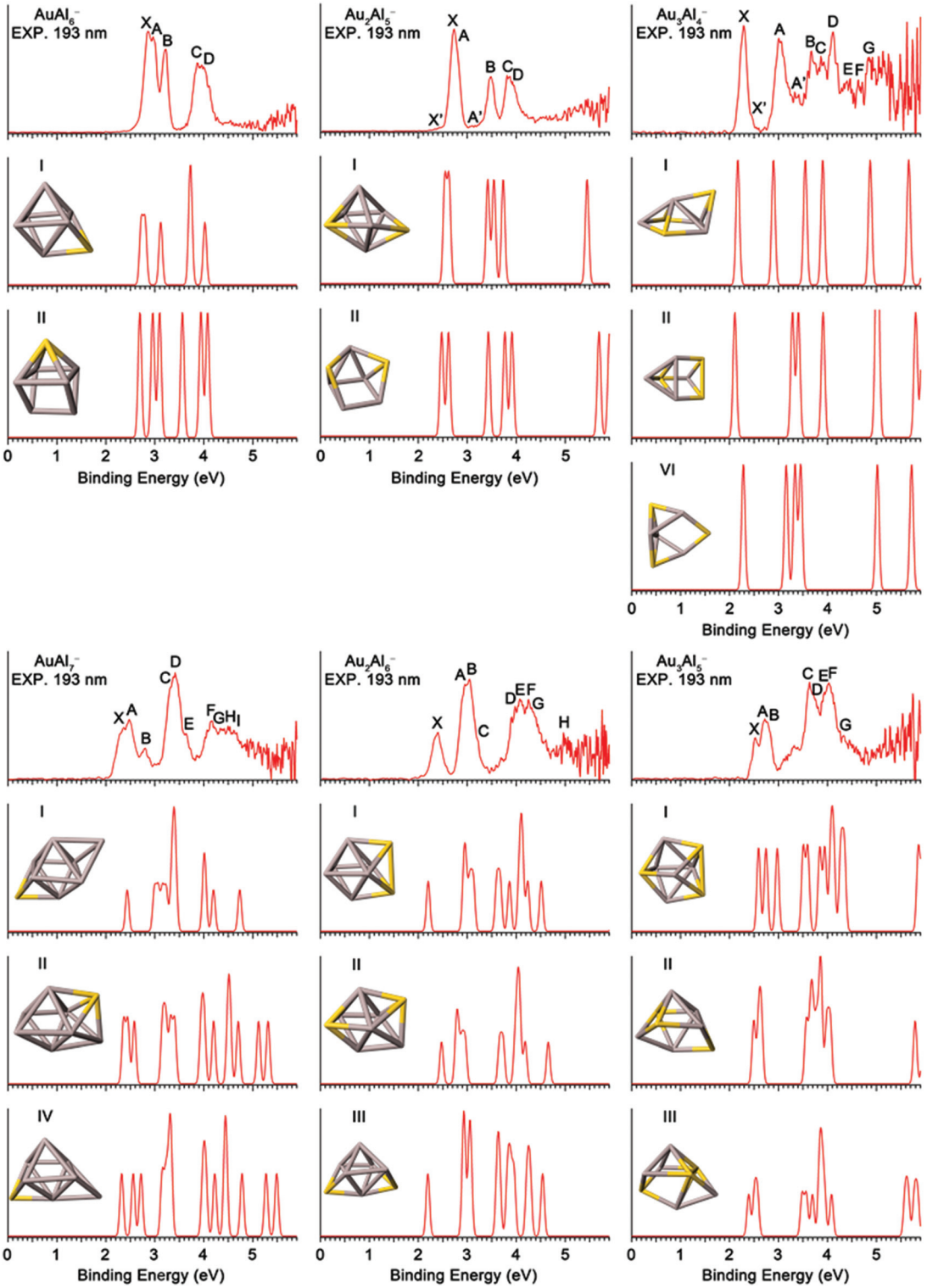

Fig. 2 Comparison of the simulated spectra for the top 2–3 low-lying isomers of $Au_xAl_y^-$ with the 193 nm experimental spectra. Atom color code: Au (gold color) and Al (grey color).

higher than isomer I) at the CCSD(T)/cc-pVTZ level of theory. The H1–H2 gap of isomer I is also much closer to the experimental value as compared to that of isomer II. All the computed VDEs of isomer I are slightly lower than the corresponding experimental values, probably due to the use of the mixed basis for computing the single-point energy at the PBE0/(Al/aug-cc-pVTZ, Au/CRENBL-ECP) level. The overall good agreement between the experiment and theory

Table 2 Theoretical VDEs, H1–H2 gap, and relative energies (ΔE) of the top six isomers of $AuAl_6^-$. Relative energies are computed at M06/aug-cc-pVDZ, M06/aug-cc-pVDZ//PBE0/mixed basis[a] and M06/aug-cc-pVDZ//CCSD(T)/cc-pVTZ levels of theory (with all isomers being optimized at the M06/aug-cc-pVDZ level). All energies are in eV

$AuAl_6^-$	ΔE (M06/aug-cc-pVDZ)	ΔE (PBE0/mixed basis[a])	ΔE (CCSD(T)/cc-pVTZ)	VDE (Theoretical)	ADE (Theoretical)	H1–H2 gap[b]
I	0	0	0	2.722	2.636	0.078
II	0.223	0.159	0.154	2.693	2.674	0.263
III	1.229	1.415	—	2.362	2.262	0.270
IV	1.231	1.471	—	2.355	—	0.305
V	1.324	1.506	—	2.432	—	0.138
VI	1.410	1.643	—	2.465	—	0.318

[a] CRENBL-ECP for Au and aug-cc-pVTZ for Al. [b] H1–H2 gap = the gap between peaks X and A.

Table 3 Theoretical VDEs, H1–H2 gap, and relative energies (ΔE) of the top ten isomers of $Au_2Al_5^-$. Relative energies are calculated at M06/aug-cc-pVDZ, M06/aug-cc-pVDZ//PBE0/mixed basis[a] and M06/aug-cc-pVDZ//CCSD(T)/cc-pVTZ levels. All energies are in eV

$Au_2Al_5^-$	ΔE (M06/aug-cc-pVDZ)	ΔE (PBE0/mixed basis[a])	ΔE (CCSD(T)/cc-pVTZ)	VDE (Theoretical)	ADE (Theoretical)	H1–H2 gap[b]
I	0	0	0	2.542	2.413	0.084
II	0.167	0.184	0.154	2.477	2.275	0.139
III	0.178	0.276	0.283	2.523	2.289	0.132
IV	0.215	0.409	—	3.381	—	0.156
V	0.284	0.321	—	2.263	—	0.279
VI	0.296	0.248	—	2.369	—	0.542
VII	0.300	0.312	—	2.314	—	0.095
VIII	0.306	0.495	—	2.531	—	0.321
IX	0.324	0.594	—	2.591	—	0.183
X	0.385	0.474	—	2.733	—	0.554

[a] CRENBL-ECP for Au and aug-cc-pVTZ for Al. [b] H1–H2 gap = the gap (in eV) between peaks X and A.

Table 4 Theoretical VDEs (in eV), H1–H2 gap (in eV) and relative energies ΔE (in eV) of the isomers of $Au_3Al_4^-$. Relative energies are calculated at M06/aug-cc-pVDZ, M06/aug-cc-pVDZ//PBE0/mixed basis[a] and M06/aug-cc-pVDZ//CCSD(T)/cc-pVTZ

$Au_3Al_4^-$	ΔE (M06/aug-cc-pVDZ)	ΔE (PBE0/mixed basis[a])	ΔE (CCSD(T)/cc-pVTZ)	VDE (Theoretical)	ADE (Theoretical)	H1–H2 gap[b]
I	0	0	0	2.167	2.073	0.729
II	0.073	0.166	0.067	2.107	—	1.178
III	0.114	0.165	0.007	1.968	1.908	1.311
IV	0.135	0.028	0.004	2.160	—	1.008
V	0.151	0.190	—	2.055	—	1.186
VI	0.177	0.115	0.134	2.281	—	0.876
VII	0.203	0.377	—	2.218	—	0.864
VIII	0.220	0.277	—	2.091	—	1.091
IX	0.345	0.318	—	2.099	—	1.153
X	0.416	0.445	—	1.920	—	1.287
XI	0.463	0.392	—	3.094	—	0.368

[a] CRENBL-ECP for Au and aug-cc-pVTZ for Al. [b] H1–H2 gap = the gap (in eV) between peaks X and A.

for $AuAl_6^-$ lends good confidence to the selected levels of theory used for other more complicated $Au_xAl_y^-$ species in the current study.

$Au_2Al_5^-$. The second panel of Fig. 2 compares the simulated spectra of the top-two low-lying isomers of $Au_2Al_5^-$ with the experimental spectrum. At all three levels of theory, *i.e.*, M06/aug-cc-pVDZ optimization, PBE0/(Al/aug-cc-pVTZ, Au/CRENBL-ECP) single-point energy, and CCSD(T)/cc-pVTZ single-point energy based on the M06 optimized structure (Table 3), isomer I is the global minimum, whereas isomer II is 0.154 eV higher at the CCSD(T) level. However, the simulated spectra of both isomers are surprisingly similar to each other, and both are in good agreement with the experimental spectrum. Thus, both isomers are likely populated experimentally. Since isomer II yielded a lower first VDE, it is more reasonable to assign it to be responsible for the weak X′ and A′ signals. This conclusion is also consistent with its relatively high energy with respect to the global minimum isomer I. Even though they give similar simulated PES spectra, isomers I and II represent different structural motifs. Isomer I retains the capped octahedron motif observed in the parent $AuAl_6^-$ and Al_7^- structures,[9,41] whereas isomer II possesses a low-

Table 5 Theoretical VDEs (in eV), H1–H2 gap (in eV) and relative energies ΔE (in eV) of the isomers of $AuAl_7^-$. Relative energies are calculated at M06/aug-cc-pVDZ, M06/aug-cc-pVDZ//PBE0/mixed basis[a] and M06/aug-cc-pVDZ//CCSD(T)/cc-pVTZ

$AuAl_7^-$	ΔE (M06/aug-cc-pVDZ)	ΔE (PBE0/mixed basis[a])	ΔE (CCSD(T)/cc-pVTZ)	VDE (Theoretical)	ADE (Theoretical)	H1–H2 gap[b]
I	0	0	0	2.434	2.175	0.556
II	0.054	0.006	0.049	2.361	2.206	0.085
III	0.072	0.113	0.128	2.721	—	0.130
IV	0.073	0.270	0.011	2.322	2.104	0.235
V	0.155	0.074	—	2.412	—	0.096
VI	0.210	0.056	—	2.490	—	0.278
VII	0.233	0.219	—	2.314	—	0.334
VIII	0.399	0.463	—	2.344	—	0.272
IX	1.008	1.043	—	2.401	—	0.231
X	1.023	1.034	—	2.648	—	0.040
XI	1.083	1.197	—	2.654	—	0.056
XII	1.207	1.181	—	2.606	—	0.066
XIII	1.214	1.249	—	2.647	—	0.026
XIV	1.291	1.306	—	2.445	—	0.062
XV	1.338	1.248	—	2.380	—	0.127

[a] CRENBL-ECP for Au and aug-cc-pVTZ for Al. [b] H1–H2 gap = the gap (in eV) between peaks X and A.

Table 6 Theoretical VDEs (in eV), H1–H2 gap (in eV) and relative energies ΔE (in eV) of the isomers of $Au_2Al_6^-$. Relative energies are calculated at M06/aug-cc-pVDZ, M06/aug-cc-pVDZ//PBE0/mixed basis[a] and M06/aug-cc-pVDZ//CCSD(T)/cc-pVTZ

$Au_2Al_6^-$	ΔE (M06/aug-cc-pVDZ)	ΔE (PBE0/mixed basis[a])	ΔE (CCSD(T)/cc-pVTZ)	VDE (theoretical)	ADE (theoretical)	H1–H2 gap[b]
I	0	0.024	0	2.201	1.884	0.730
II	0.104	0	0.003	2.475	2.048	0.300
III	0.137	0.095	0.151	2.195	1.872	0.732
IV	0.154	0.131	—	2.556	—	0.340
V	0.475	0.493	—	2.459	—	0.188
VI	0.584	0.660	—	2.391	—	0.483
VII	0.595	0.741	—	2.755	—	0.199

[a] CRENBL-ECP for Au and aug-cc-pVTZ for Al. [b] H1–H2 gap = the gap (in eV) between peaks X and A.

Table 7 Theoretical VDEs (in eV), H1–H2 gap (in eV) and relative energies ΔE (in eV) of the isomers of $Au_3Al_5^-$. Relative energies are calculated at M06/aug-cc-pVDZ, M06/aug-cc-pVDZ//PBE0/mixed basis[a] and M06/aug-cc-pVDZ//CCSD(T)/cc-pVTZ

$Au_3Al_5^-$	ΔE (M06/aug-cc-pVDZ)	ΔE (PBE0/mixed basis[a])	ΔE (CCSD(T)/cc-pVTZ)	VDE (Theoretical)	ADE (Theoretical)	H1–H2 gap[b]
I	0	0.016	0	2.593	2.385	0.151
II	0.054	0	0.009	2.495	2.352	0.103
III	0.066	0.077	0.002	2.391	2.380	0.118
IV	0.079	0.359	—	2.609	—	0.002
V	0.126	0.437	—	2.582	—	0.225
VI	0.191	0.434	—	2.722	—	0.030

[a] CRENBL-ECP for Au and aug-cc-pVTZ for Al. [b] H1–H2 gap = the gap (in eV) between peaks X and A.

symmetry C_s open cage-like structure that has never been observed in either pure Al or Au clusters in such small-sized ranges.

$Au_3Al_4^-$. The CCSD(T)/cc-pVTZ relative energies (Table 4) show that isomers I, II, III and IV are nearly degenerate and are competing for the global minimum, while isomer (VI) is 0.134 eV higher in energy than isomer I. Isomer I gives an H1–H2 gap of 0.729 eV, very close to the experimental value of 0.71 eV. The presence of features like X, A, B, D and G and the lowest M06/aug-cc-pVDZ, PBE0/(Al/aug-cc-pVTZ, Au/CRENBL-ECP) and CCSD(T)/cc-pVTZ relative energies make isomer I a good choice for the major contributor towards the experimental spectra. Isomers II, III and IV can be excluded as their H1–H2 gaps are larger than the experimental value and peak X in the experimental spectra shows no front tails. Similar to the case of $Au_2Al_5^-$, where isomer II's energy is 0.154 eV higher than isomer I at the CCSD(T) level and it turns out to be a minor contributor, the isomer VI of $Au_3Al_4^-$ is higher in energy than isomer I by 0.134 eV at the CCSD(T) level but the simulated spectrum of isomer VI can well reproduce the bands X′ and A′, thereby suggesting that isomer VI might be a minor contributor to the observed spectrum. The peaks C, E and G

seem to be missing in the case of both isomers I and VI, indicating the contribution from more isomers or multi-electron processes. Overall, isomer I is the global minimum structure and isomer VI is a minor isomer for the observed spectrum.

$AuAl_7^-$. The CCSD(T)/cc-pVTZ relative energies (Table 5) show that isomer I of $AuAl_7^-$ is the global minimum, while the relative energies of isomers II and IV are only slightly higher than that of isomer I. The simulated PES spectra of isomers I, II, and IV are compared with the experiment in the fourth panel of Fig. 2. The simulated spectra of both isomers II and IV are similar and both are in good agreement with the experimental spectra. The simulated spectrum of isomer I also displays features similar to the experimental spectrum, which was complicated with hints of multiple isomers. Hence, we cannot definitely conclude that either isomer II or IV is the global minimum due to their close energies at the current levels of theory. Isomer IV has been reported as the global minimum of $AuAl_7^-$ in a previous DFT study.[17]

$Au_2Al_6^-$. In the case of $Au_2Al_6^-$, both isomers I and III give similar simulated spectra (see the fifth panel of Fig. 2), which are in good agreement with the experimental spectrum. The M06/aug-cc-pVDZ and CCSD(T)/cc-pVTZ relative energies of isomer I are lower than that of isomers II and III. The PBE0/(Al/aug-cc-pVTZ, Au/CRENBL-ECP) relative energies (see Table 6) of all three isomers are almost degenerate, with isomer II being slightly more stable. Based on the comparison between the simulated and experimental PES spectrum and the relative energy data, isomer I with the D_{2d}-docahedra structure (which can be formed by a small distortion from the *cis*-bicapped octahedron) can be considered as the best candidate in this case. Isomer II can be ruled out as the H1–H2 gap is much smaller than the corresponding experimental gap. As isomer III has a 0.151 eV CCSD(T)/cc-pVTZ relative energy, it can be considered only as a minor isomer in this case.

$Au_3Al_5^-$. For $Au_3Al_5^-$, the top-three low-lying isomers are almost degenerate at both DFT and CCSD(T) (Table 7) levels of theory. As seen in the sixth panel of Fig. 2, the simulated spectra of both isomers II and III contain the peaks X–F of the experimental spectrum. In the case of isomer I (which can be viewed as a small distortion from the *cis*-bicapped octahedron), peaks C and D appear to be absent, however, its simulated spectrum seems to contain the weak features between bands B and C. Based on these observations, it can be concluded that isomers II and III of $Au_3Al_5^-$ are competing for the global minimum, while isomer I can be considered as a minor contributor.

4 Discussion and conclusion

The identified global-minima (including major and minor) isomers of the $Au_xAl_y^-$ ($x + y = 7,8$; $x = 1–3$; $y = 4–7$) alloy clusters are shown in Fig. 3, along with those of bare Al_x^- ($x = 6–8$) for comparison. Note that previous studies have shown that Al_6^- exhibits the square bi-pyramidal structure due to a Jahn–Teller distortion from the O_h symmetry, and can be viewed as a magic-number cluster or motif. Indeed, this structural motif is also present in the structures of Al_7^- and Al_8^- (highlighted in green in Fig. 3).[35] Interestingly, the Al_6^- motif is also seen in a number of global minimum structures in the $Au_xAl_y^-$ alloy clusters (see the green highlight in Fig. 3). As reported previously, the Al_6^- motif remains intact in $AuAl_6^-$.[9] In fact, the structures of $AuAl_6^-$ and Al_7^- are exactly the same except that the capping Al atom in Al_7^- is replaced by Au in $AuAl_6^-$. A distorted square bi-pyramid motif due to the presence of two Au atoms can be observed in the case of $Au_2Al_5^-$. As the number of Al atoms is reduced to four, the assigned structures for $Au_3Al_4^-$ no longer display any trace of the square

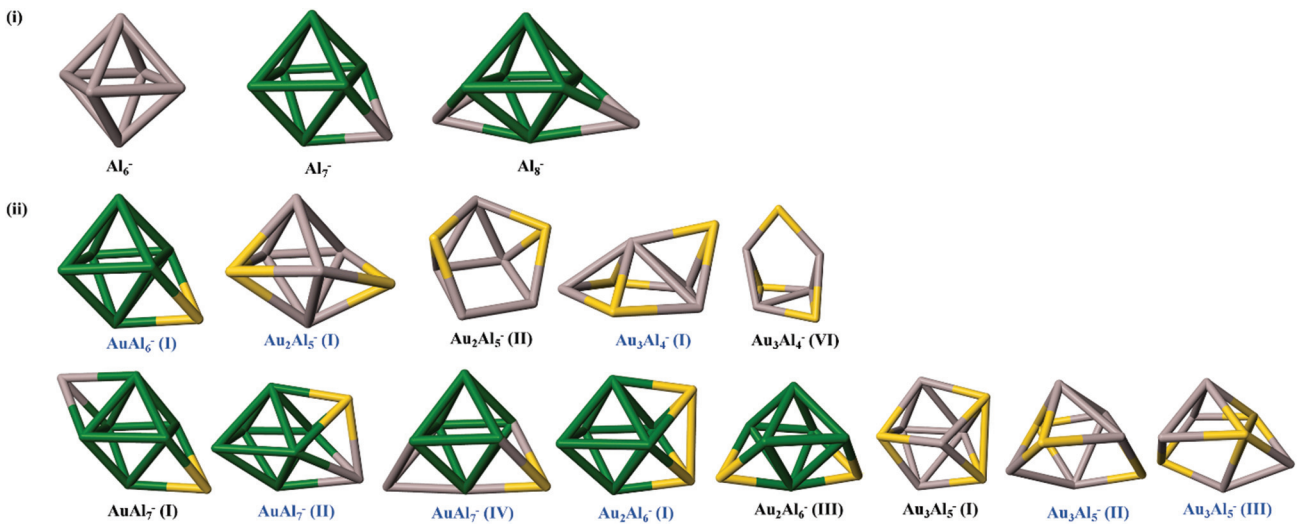

Fig. 3 (i) Previously reported structures of Al_6^-, Al_7^- and Al_8^- (ii) assigned global minimum (including major and minor) isomers of $AuAl_6^-$, $Au_2Al_5^-$, $Au_3Al_4^-$, $AuAl_7^-$, $Au_2Al_6^-$ and $Au_3Al_5^-$. The major isomers for each cluster are denoted by the blue text below the plotted structure. Atom color code: Au (gold color) and Al (grey or green color). The Al atoms in green color highlight the highly stable square bi-pyramidal Al_6^- motif.

bi-pyramid motif. In other words, the replacement of three aluminum atoms with gold atoms in the 7-atom gold–aluminum alloy cluster completely disrupts the square bi-pyramidal motif.

A similar trend can be observed in the 8-atom alloy clusters, with increasing Au compositions from $AuAl_7^-$ to $Au_3Al_5^-$. First, in all the three assigned isomers of $AuAl_7^-$, the square bi-pyramidal Al_6^- motif is observed. The isomer IV of $AuAl_7^-$ has the same structure as Al_8^- except that one of the Al atoms capping one of the faces of the square bi-pyramid is replaced by an Au atom in the case of the major isomer of $AuAl_7^-$. Second, in the assigned isomer of $Au_2Al_6^-$, the square bi-pyramidal structure of the Al_6^- unit is still intact, indicating the high robustness of the Al_6^- motif even under the influence of two "foreign" Au atoms. Here, the two Au atoms cap the upper and lower faces on same side of Al_6^-, respectively. Finally, it is somewhat surprising to see that the structures of both the assigned major isomers of the $Au_3Al_5^-$ cluster contain a highly distorted square bi-pyramidal motif, with isomer II bearing some resemblance to the assigned isomer IV of $AuAl_7^-$. Hence, even under the influence of three "foreign" Au atoms, it seems that the tendency to form the square bi-pyramidal structure with the remaining five Al atoms still prevails. Overall, it appears that when the Al component is more dominant than the Au component, *i.e.*, for $y > x$, in $Au_xAl_y^-$ ($x + y = 7,8$), the tendency to form the square bi-pyramidal structure dominates, suggesting that the Al–Al interaction out-performs the Au–Au interaction. As such, for $x > 1$, the gold atoms tend to be separated by Al atoms unless only the magic-number Al_6^- square bi-pyramid motif is present.

In conclusion, combined photoelectron spectroscopy and DFT theoretical studies of a series of gold–aluminum alloy clusters, $Au_xAl_y^-$ ($x + y = 7,8$; $x = 1$–3; $y = 4$–7), are reported. The experimental photoelectron spectra obtained at various photon energies revealed well-resolved spectral features, which are used to compare with the simulated spectra of low-lying isomers. The BH global optimization combined with DFT calculations was used for structural searches. A good agreement between the experimental and simulated spectra, as well as relative energies derived at both DFT and CCSD(T) levels of theory, helps the identification of the global minimum and possible low-lying isomers for each cluster. Several important structural patterns of the Au–Al alloy clusters are identified from the comprehensive study. Notably, for $y \geq 6$ in $Au_xAl_y^-$ clusters, the all-aluminum square bi-pyramidal motif is highly robust. So when the Al component is more dominant than the Au component, *i.e.*, for $y > x$, in $Au_xAl_y^-$ ($x + y = 7,8$), a strong tendency to form the square bi-pyramidal structure prevails, suggesting that the Al–Al interaction dominates the Au–Au interaction. A closely related trend is that for $x > 1$, the gold atoms tend to be separated by Al atoms unless only the magic-number Al_6^- square bi-pyramid motif is present. In other words, in the small-sized mixed clusters, Al and Au components do not mix that well. Al component appears to play a more dominant role due to the high robustness of the magic-number Al_6^- square bi-pyramid motif, whereas the Au component tends to be either "adsorbed" onto the Al_6^- square bi-pyramid motif if $y > 6$, or stays away from one another if $x < y < 6$.

Acknowledgements

The experimental work done at Brown University was supported by the National Science Foundation (CHE-1263745). The theoretical work done at the University of Nebraska was supported by the UNL Nebraska Center for Energy Sciences and Holland Computing Center.

References

1 F. Furche, R. Ahlrichs, P. Weis, C. Jacob, S. Gilb, T. Bierweiler and M. M. Kappes, *J. Chem. Phys.*, 2002, **117**, 6982–6990.
2 B. K. Rao and P. Jena, *J. Chem. Phys.*, 1999, **111**, 1890–1904.
3 S. Bulusu, X. Li, L.-S. Wang and X. C. Zeng, *Proc. Natl. Acad. Sci. U. S. A.*, 2006, **103**, 8326–8330.
4 G. Chen, Q. Wang, Q. Sun, Y. Kawazoe and P. Jena, *J. Chem. Phys.*, 2010, **132**, 194306.
5 J. Li, X. Li, H.-J. Zhai and L.-S. Wang, *Science*, 2003, **299**, 864–867.
6 W. Huang, S. Bulusu, R. Pal, X. C. Zeng and L.-S. Wang, *ACS Nano*, 2009, **3**, 1225–1230.
7 W. Bouwen, F. Vanhoutte, F. Despa, S. Bouckaert, S. Neukermans, L. Theil Kuhn, H. Weidele, P. Lievens and R. E. Silverans, *Chem. Phys. Lett.*, 1999, **314**, 227–233.
8 M. Heinebrodt, N. Malinowski, F. Tast, W. Branz, I. M. L. Billas and T. P. Martin, *J. Chem. Phys.*, 1999, **110**, 9915–9921.
9 A. E. Kuznetsov, A. I. Boldyrev, H.-J. Zhai, X. Li and L.-S. Wang, *J. Am. Chem. Soc.*, 2002, **124**, 11791–11801.
10 C. Majumder, A. K. Kandalam and P. Jena, *Phys. Rev. B*, 2006, **74**, 205437.
11 M. L. Kimble, A. W. Castleman, J. U. Reveles and S. N. Khanna, *Collect. Czech. Chem. Commun.*, 2007, **72**, 185–196.
12 R. Pal, L.-F. Cui, S. Bulusu, H.-J. Zhai, L.-S. Wang and X. C. Zeng, *J. Chem. Phys.*, 2008, **128**, 024305.
13 M.-X. Chen, X. H. Yan and S. Wei, *J. Phys. Chem. A*, 2007, **111**, 8659–8662.
14 C.-J. Wang, X.-Y. Kuang, H.-Q. Wang, H.-F. Li, J.-B. Gu and J. Liu, *Comput. Theor. Chem.*, 2012, **1002**, 31–36.
15 Y.-F. Li, A.-J. Mao, Y. Li and X.-Y. Kuang, *J. Mol. Model.*, 2012, **18**, 3061–3072.
16 Y.-F. Li, Y. Li and X.-Y. Kuang, *Eur. Phys. J. D*, 2013, **67**, 132.
17 S. Y. Li, L. Guo, R. J. Zhang and X. Zhang, *J. Struct. Chem.*, 2014, **55**, 612–620.
18 G. V. Lopez, J. Czekner, T. Jian, W.-L. Li, Z. Yang and L.-S. Wang, *J. Chem. Phys.*, 2014, **141**, 224309.
19 J.-Y. Zhao, Y. Zhang, F.-Q. Zhao and X.-H. Ju, *J. Phys. Chem. A*, 2013, **117**, 12519–12528.

20 J. C. Smith, A. C. Reber, S. N. Khanna and A. W. Castleman, *J. Phys. Chem. A*, 2014, **118**, 8485–8492.
21 C. Rajesh and C. Majumder, *J. Chem. Phys.*, 2009, **130**, 234309.
22 X.-J. Feng and Y.-H. Luo, *J. Phys. Chem. A*, 2007, **111**, 2420–2425.
23 X. Li, A. E. Kuznetsov, H.-F. Zhang, A. I. Boldyrev and L.-S. Wang, *Science*, 2001, **291**, 859–861.
24 A. E. Kuznetsov, K. A. Birch, A. I. Boldyrev, X. Li, H.-J. Zhai and L.-S. Wang, *Science*, 2003, **300**, 622–625.
25 K. Koyasu, Y. Naono, M. Akutsu, M. Mitsui and A. Nakajima, *Chem. Phys. Lett.*, 2006, **422**, 62–66.
26 J. J. Gu, J. X. Yang and D. Dong, *Physica B*, 2008, **403**, 4033–4037.
27 L.-M. Wang, S. Bulusu, H.-J. Zhai, X.-C. Zeng and L.-S. Wang, *Angew. Chem., Int. Ed.*, 2007, **46**, 2915–2918.
28 L.-M. Wang, R. Pal, W. Huang, X. C. Zeng and L.-S. Wang, *J. Chem. Phys.*, 2009, **130**, 051101.
29 R. Pal, L.-M. Wang, W. Huang, L.-S. Wang and X. C. Zeng, *J. Am. Chem. Soc.*, 2009, **131**, 3396–3404.
30 L. S. Wang, H. S. Cheng and J. Fan, *J. Chem. Phys.*, 1995, **102**, 9480–9493.
31 J. P. Perdew, K. Burke and M. Ernzerhof, *Phys. Rev. Lett.*, 1996, **77**, 3865–3868.
32 B. Delley, *J. Chem. Phys.*, 1990, **92**, 508–517.
33 B. Delley, *J. Chem. Phys.*, 2000, **113**, 7756–7764.
34 Y. Zhao and D. G. Truhlar, *Theor. Chem. Acc.*, 2008, **120**, 215–241.
35 T. H. Dunning Jr., *J. Chem. Phys.*, 1989, **90**, 1007–1023.
36 M. J. Frisch, G. W. Trucks, H. B. Schlegel, G. E. Scuseria, M. A. Robb, J. R. Cheeseman, G. Scalmani, V. Barone, B. Mennucci, G. A. Petersson, H. Nakatsuji, M. Caricato, X. Li, H. P. Hratchian, A. F. Izmaylov, J. Bloino, G. Zheng, J. L. Sonnenberg, M. Hada, M. Ehara, K. Toyota, R. Fukuda, J. Hasegawa, M. Ishida, T. Nakajima, Y. Honda, O. Kitao, H. Nakai, T. Vreven, J. A. Montgomery Jr., J. E. Peralta, F. Ogliaro, M. Bearpark, J. J. Heyd, E. Brothers, K. N. Kudin, V. N. Staroverov, R. Kobayashi, J. Normand, K. Raghavachari, A. Rendell, J. C. Burant, S. S. Iyengar, J. Tomasi, M. Cossi, N. Rega, J. M. Millam, M. Klene, J. E. Knox, J. B. Cross, V. Bakken, C. Adamo, J. Jaramillo, R. Gomperts, R. E. Stratmann, O. Yazyev, A. J. Austin, R. Cammi, C. Pomelli, J. W. Ochterski, R. L. Martin, K. Morokuma, V. G. Zakrzewski, G. A. Voth, P. Salvador, J. J. Dannenberg, S. Dapprich, A. D. Daniels, O. Farkas, J. B. Foresman, J. V. Ortiz, J. Cioslowski and D. J. Fox, *Gaussian 09 Revision D.01*, Gaussian Inc., Wallingford, CT, 2009.
37 C. Adamo and V. Barone, *J. Chem. Phys.*, 1999, **110**, 6158–6169.
38 M. Valiev, E. J. Bylaska, N. Govind, K. Kowalski, T. P. Straatsma, H. J. J. Van Dam, D. Wang, J. Nieplocha, E. Apra, T. L. Windus and W. A. de Jong, *Comput. Phys. Commun.*, 2010, **181**, 1477–1489.
39 G. D. Purvis III and R. J. Bartlett, *J. Chem. Phys.*, 1982, **76**, 1910–1918.
40 R. A. Kendall, T. H. Dunning Jr. and R. J. Harrison, *J. Chem. Phys.*, 1992, **96**, 6796–6806.
41 S. Paranthaman, K. Hong, J. Kim, D. E. Kim and T. K. Kim, *J. Phys. Chem. A*, 2013, **117**, 9293–9303.